

Different radial basis functions and their applicability for regional gravity field representation on the sphere

Katrin Bentel · Michael Schmidt ·
Christian Gerlach

Received: 17 September 2012 / Accepted: 12 December 2012 / Published online: 3 February 2013
© Springer-Verlag Berlin Heidelberg 2013

Abstract Global gravity field solutions are commonly modelled in spherical harmonic basis functions. Additionally, radial basis functions on the sphere with quasi-local support are used to model regional refinements of gravity fields. However, these functions are usually not orthogonal on a sphere, which makes the modelling process more complex. In this paper we study and compare different radial basis functions and their performance in regional gravity field modelling on the sphere by making use of simulated data. In addition to the type of radial basis function also the size of the study area on the sphere, the point grid, the margins and the method which is used to solve the singular system have to be taken into account. The synthetic signal, which we use in our simulation, is a residual signal in a bandwidth which corresponds to the bandwidth of GOCE satellite gravity observations.

Keywords Radial basis function · Regional gravity field modelling · Singular problem

Mathematics Subject Classification 86A30 · 86A22

K. Bentel (✉)

Department of Mathematical Sciences and Technology,
IMT, Norwegian University of Life Sciences, Postboks 5003, 1432 Ås, Norway
e-mail: katrin.bentel@gmail.com

M. Schmidt

Deutsches Geodätisches Forschungsinstitut, Munich, Germany

C. Gerlach

Bavarian Academy of Sciences and Humanities,
Commission of Geodesy and Glaciology, Munich, Germany

1 Introduction

Global Earth gravity models are commonly represented in spherical harmonic basis functions. These global models can be regionally refined by additional satellite, airborne, or terrestrial gravity measurements. Spherical harmonic basis functions, which are globally oscillating functions, provide no spatial localization and therefore regional refinements of the gravity field on the sphere cannot be represented in an optimal way. If the signal varies in only one point on the sphere, in such a representation, the whole global solution has to change, since they are globally-optimized best-fit solutions. Small spatial details are difficult to represent and can even be masked in the solutions.

In contrast to spherical harmonics, spherical radial basis functions provide quasi-compact support. Their influence decreases rapidly with distance from their center. Thus, they are very appropriate to model regional detailed refinements to global gravity models. The synthetic example signal we use to test different modelling scenarios in spherical radial basis functions is such a regional detailed gravity signal, from spherical harmonic degrees 150–250, which corresponds to the sensitive bandwidth of gravity measurements taken by the GOCE (Gravity Field and Steady-State Ocean Circulation Explorer) satellite gravity mission, see [ESA \(1999\)](#).

Various different approaches for regional gravity modelling on the sphere in radial basis functions have already been investigated. Foundations on radial basis function on the sphere can be found for example in [Freeden et al. \(1998\)](#), [Holschneider et al. \(2003\)](#), [Freeden and Michel \(2004\)](#), or [Chambodut et al. \(2005\)](#). Examples and explanations for application to regional gravity field modelling can be found, amongst many others, in [Freeden and Schreiner \(2005\)](#), [Tenzer and Klees \(2007\)](#), [Schmidt et al. \(2007\)](#), [Klees et al. \(2008\)](#), and the references therein. Details for the derivation of regional gravity solutions from other gravity functionals through modelling in radial basis functions are given in [Freeden et al. \(2009\)](#) or in [Wolf \(2009\)](#). [Freeden and Schreiner \(2006\)](#) describe regional modelling of geoid heights from deflections of the vertical through the appropriate choice of the radial basis function, and in [Fehlinger \(2009\)](#) detailed derivations for regional gravity modelling from deflections of the vertical can be found. [Gerhards \(2012\)](#) and [Fehlinger et al. \(2007\)](#) use radial basis functions for regional modelling of the geomagnetic field and the sea surface topography. Within the aforementioned references mostly numerical integration methods are used for regional signal representation. In contrast to these investigations we will use in the following parameter estimation methods. This allows to take observation errors into account and to assess the quality of the estimated coefficients. The approach is also suitable to combine different types of observations—this is, however, not part of the current investigations. In order to compare different radial basis functions in detail, and evaluate their performance in regional gravity representations, we use a set of different radial basis functions and test them on a synthetic data set under the same conditions. All radial basis functions we investigate can be represented in an expansion in Legendre polynomials. They represent a compromise between the two extreme cases, the Dirac delta impulse and spherical harmonics. The first has the property of optimal spatial localization but no frequency localization. In contrast, the latter has optimal frequency, but no spatial localization properties. Based on an analysis

of strength and shortcomings of the different functions we try to find the optimal compromise for the purpose of regional gravity field modelling. However, it is not only the choice of the radial basis function which plays an important role, but also the point grid on which the functions are placed, the size of the area to be represented, the margin widths around the area, as well as the method which is used to determine the coefficients of the representation in spherical radial basis functions. All these aspects together with the choice of the radial basis function are considered in the simulations.

In contrast to Klees et al. (2008), Antoni et al. (2009) and Fischer (2011), who have developed non-linear algorithms to optimize the different parameters simultaneously, we choose the point grids and type of basis functions for each simulation scenario and use parameter estimation in a second step to determine the coefficients in the representation. Because the system of observation equations is singular, the quality of the regional approximation strongly depends on the estimation method applied. We compare two such methods, a truncated singular value decomposition and a regularization using prior information.

Sections 2–4 review gravity field modelling in spherical harmonic and spherical radial basis functions. Section 5 gives an explanation of the singularities in the linear equation system and introduces the two applied estimation methods. The discussion of the different basis functions and their performance in gravity field modelling from several simulation scenarios is presented in Sect. 6. Finally, Sect. 7 summarizes the results.

2 Gravity field modelling in spherical harmonics

Let the position vector of any arbitrary point on a sphere Ω_r with radius r be denoted by \mathbf{x} and in spherical coordinates given by

$$\mathbf{x} = r [\cos \phi \cos \lambda, \cos \phi \sin \lambda, \sin \phi]' = r \mathbf{r}. \quad (1)$$

Hereby is ϕ the latitude, λ the longitude, r the distance from center of the sphere, and \mathbf{r} the unit vector in direction of \mathbf{x} .

2.1 Spherical harmonics

A function which fulfills the Laplace equation, $\Delta F(\mathbf{x}) = 0$, in the exterior of a sphere Ω_R , with radius R , e.g. R —mean Earth radius, can be represented on Ω_R in spherical harmonic basis functions, $Y_{nm}^R(\mathbf{x})$, as

$$F(\mathbf{x}) = \sum_{n=0}^{\infty} \sum_{m=-n}^n F_{nm} Y_{nm}^R(\mathbf{x}). \quad (2)$$

The surface spherical harmonics, $Y_{nm}(\mathbf{x})$, on Ω_R of degree n and order m , are defined as

$$Y_{nm}(\mathbf{x}) = \frac{1}{R\sqrt{4\pi}} \begin{cases} \bar{P}_{nm}(\sin \phi) \cos m\lambda & \text{for } m = 0, 1, 2, \dots, n \\ \bar{P}_{n|m|}(\sin \phi) \sin |m|\lambda & \text{for } m = -n, \dots, -2, -1 \end{cases} \quad (3)$$

$$\text{and } Y_{nm}^R(\mathbf{x}) = \frac{1}{R} Y_{nm}(\mathbf{x}), \quad (4)$$

$\bar{P}_{nm}(\sin \phi)$ are the fully normalized Legendre functions.

For details on spherical harmonics see [Hofmann-Wellenhof and Moritz \(2005\)](#) or [Moritz \(1989\)](#). Two important properties shall be noted here:

1. Addition theorem of spherical harmonics

$$\frac{2n+1}{4\pi} P_n(\mathbf{r}'_p \mathbf{r}_q) = \sum_{m=-n}^n Y_{nm}(\mathbf{x}_p) Y_{nm}(\mathbf{x}_q) \quad (5)$$

This theorem connects spherical harmonics and Legendre polynomials P_n .

2. Orthogonality relation

$$\begin{aligned} \frac{1}{R^2} \int_{\Omega_R} Y_{nm}(\mathbf{x}) Y_{kl}(\mathbf{x}) d\omega &= \delta_{n,k} \delta_{m,l} \\ d\omega &= R^2 \cos \phi d\phi d\lambda \\ \delta_{n,k} &= \begin{cases} 1 & \text{for } k = n \\ 0 & \text{for } k \neq n \end{cases} \end{aligned} \quad (6)$$

Thus, a function $F(\mathbf{x})$ on the sphere Ω_R has a unique representation in the form of Eq. (2), where the spherical harmonics $Y_{nm}(\mathbf{x})$ form an orthonormal basis.

2.2 Up- and downward continuation of the gravitational potential

In case F is the gravitational potential, up- and downward continuation of the potential play a very important role.

The following expression gives the representation of a potential F on a point \mathbf{x}_p outside a sphere Ω_R :

$$F(\mathbf{x}_p) = \sum_{n=0}^{\infty} \sum_{m=-n}^n \left(\frac{R}{r}\right)^{n+1} F_{nm} Y_{nm}^R(\mathbf{x}_p) \quad (7)$$

with $r = |\mathbf{x}_p|$ (geocentric radius of the computation point \mathbf{x}_p) and $r \geq R$, the term $\left(\frac{R}{r}\right)^{n+1}$ allows for harmonic continuation into the exterior of the sphere Ω_R . From $\lim_{r \rightarrow \infty} \frac{R}{r} = 0$ follows $\lim_{r \rightarrow \infty} F = 0$ and Eq. (7) also holds for points on the sphere, since for $r = R$ it leads to Eq. (2).

2.3 Determination of the Stokes coefficients

Since any harmonic function on a sphere Ω_R has a unique expansion into a series according to (2), the coefficients F_{nm} can be computed by the **spherical Fourier transform**:

$$F_{nm} = \int_{\Omega_R} F(\mathbf{x}) Y_{nm}^R(\mathbf{x}) d\omega \quad (8)$$

$\mathbf{x} \in \Omega_R$, and $d\omega$ denotes the surface element on the sphere, see Eq. (6).

A **numerical evaluation of the integration** is possible for example with

$$F_{nm} = \int_{\Omega_R} F(\mathbf{x}) Y_{nm}^R(\mathbf{x}) d\omega \approx \sum_{i=1}^N F(\mathbf{x}_i) Y_{nm}^R(\mathbf{x}_i) w_i \quad (9)$$

where w_i are integration weights.

Another method to determine the coefficients F_{nm} is **parameter estimation**. Its benefits in comparison to numerical integration are given below.

The representation of an observed signal F with error e in spherical harmonics

$$F(\mathbf{x}) + e(\mathbf{x}) = \sum_{n=0}^N \sum_{m=-n}^n F_{nm} Y_{nm}^R(\mathbf{x}) \quad (10)$$

leads to the observation equation

$$\mathbf{l} + \mathbf{e} = \mathbf{A} \cdot \mathbf{f} \quad (11)$$

$$\begin{bmatrix} F(\mathbf{x}_1) \\ F(\mathbf{x}_2) \\ \vdots \\ F(\mathbf{x}_L) \end{bmatrix} + \begin{bmatrix} e(\mathbf{x}_1) \\ e(\mathbf{x}_2) \\ \vdots \\ e(\mathbf{x}_L) \end{bmatrix} = \begin{bmatrix} Y_{0,0}^R(\mathbf{x}_1) & \cdots & Y_{N,N}^R(\mathbf{x}_1) \\ \vdots & \ddots & \vdots \\ Y_{0,0}^R(\mathbf{x}_L) & \cdots & Y_{N,N}^R(\mathbf{x}_L) \end{bmatrix} \cdot \begin{bmatrix} F_{0,0} \\ F_{1,-1} \\ \vdots \\ F_{N,N} \end{bmatrix}$$

with the stochastic model

$$D(\mathbf{l}) = \sigma_0^2 \mathbf{P}^{-1}. \quad (12)$$

Hereby, σ_0^2 is the unknown variance factor and \mathbf{P} is the given positive definite weight matrix for the observations. It contains the weights of the observations on the diagonal and the correlations can be derived from the covariance matrix \mathbf{P}^{-1} , see Koch (1999). The error vector \mathbf{e} comprises observation errors, modelling errors, and truncation errors. The truncation error is caused by limiting the functional model (10) to a maximum degree N , such that non band-limited signals cannot be completely represented. Least squares estimation with $\mathbf{e}^T \mathbf{e} \rightarrow \min$ yields the estimated coefficients $\hat{\mathbf{f}}$, if the normal equation matrix $\mathbf{A}^T \mathbf{P} \mathbf{A}$ is regular, with

$$\hat{\mathbf{f}} = (\mathbf{A}^T \mathbf{P} \mathbf{A})^{-1} \mathbf{A}^T \mathbf{P} \mathbf{l} \quad (13)$$

If $(\mathbf{A}^T \mathbf{P} \mathbf{A})^{-1}$ exists, then the point grid for the observations is admissible and it holds $L \geq (N+1)^2$ for the number of observations L and the number of unknowns $(N+1)^2$.

Then parameter estimation is an appropriate procedure because of the overdetermination of the system. For $L = (N + 1)^2$ the point system is fundamental and the parameters to be determined are unique. All point grids we use later in our examples are admissible.

The covariance matrix for the estimated parameters, $\hat{\sigma}_0^2 \mathbf{Q}$, is determined by

$$\hat{\sigma}_0^2 \mathbf{Q} = \hat{\sigma}_0^2 (\mathbf{A}^T \mathbf{P} \mathbf{A})^{-1} \quad (14)$$

with the estimated variance factor

$$\hat{\sigma}_0^2 = \frac{\hat{\mathbf{e}}^T \mathbf{P} \hat{\mathbf{e}}}{L - (N + 1)^2} \quad (15)$$

and $\hat{\mathbf{e}} = \mathbf{A} \hat{\mathbf{f}} - \mathbf{l}.$

The main advantages of parameter estimation compared to numerical integration techniques are that (1) estimates of the errors of the parameters and the corresponding correlations can be derived and (2) observations $F(\mathbf{x})$ may be of different types and can be given at any location, i.e. no grid is necessary. In contrast, numerical integration as in Eq. (9) requires the data $F(\mathbf{x}_i)$ to be given on a regular grid (standard grid, Reuter grid, icosahedron grid, ...) and, see Eq. (9), the integration weights have to be known. In most cases the original observations have to be interpolated in order to compute the numerical integration.

3 Gravity field modelling in spherical radial basis functions

3.1 From spherical harmonics to radial basis functions with local support

The potential outside a sphere, as it was given in Eq. (7), can be reformulated using Eqs. (8) and (5):

$$F(\mathbf{x}) = \sum_{n=0}^{\infty} \sum_{m=-n}^n \left(\frac{R}{r}\right)^{n+1} F_{nm} Y_{nm}^R(\mathbf{x}) \quad (16)$$

$$= \sum_{n=0}^{\infty} \sum_{m=-n}^n \left(\frac{R}{r}\right)^{n+1} \int_{\Omega_R} F(\mathbf{x}_p) Y_{nm}^R(\mathbf{x}_p) d\omega Y_{nm}^R(\mathbf{x}) \quad (17)$$

$$= \int_{\Omega_R} F(\mathbf{x}_p) \sum_{n=0}^{\infty} \left(\frac{R}{r}\right)^{n+1} \sum_{m=-n}^n Y_{nm}^R(\mathbf{x}_p) Y_{nm}^R(\mathbf{x}) d\omega \quad (18)$$

$$= \int_{\Omega_R} F(\mathbf{x}_p) \sum_{n=0}^{\infty} \frac{2n+1}{4\pi R^2} \left(\frac{R}{r}\right)^{n+1} P_n(\mathbf{r}' \mathbf{r}_p) d\omega \quad (19)$$

Defining a kernel as

$$k(\mathbf{x}, \mathbf{x}_p) = \sum_{n=0}^{\infty} \frac{2n+1}{4\pi R^2} \left(\frac{R}{r}\right)^{n+1} P_n(\mathbf{r}'\mathbf{r}_p) \quad (20)$$

leads to:

$$F(\mathbf{x}) = \int_{\Omega_R} k(\mathbf{x}, \mathbf{x}_p) F(\mathbf{x}_p) d\omega \quad (21)$$

$$= (k * F)_{\Omega_R}(\mathbf{x}) \quad \mathbf{x}_p \in \Omega_R; \quad \mathbf{x} \in \overline{\Sigma_R^{\text{ext}}} \quad (22)$$

which is the **convolution** formula with reproducing kernel k .

A convolution kernel can be generally expressed as

$$B(\mathbf{x}, \mathbf{x}_p) = \sum_{n=0}^{\infty} \frac{2n+1}{4\pi R^2} \left(\frac{R}{r}\right)^{n+1} B_n P_n(\mathbf{r}'\mathbf{r}_p), \quad (23)$$

where the coefficients B_n actually define the kernel and reflect its frequency behavior. For the reproducing kernel above in Eq. (20) it holds $B_n = 1 \forall n$.

Later on, we use radial basis functions defined on the unit sphere. Therefore, on the unit sphere, where $R = r = 1$, the general kernel reads

$$B(\mathbf{x}, \mathbf{x}_p) = \sum_{n=0}^{\infty} \frac{2n+1}{4\pi} B_n P_n(\mathbf{r}'\mathbf{r}_p). \quad (24)$$

With $\mathbf{r}'\mathbf{r}_p = \cos \alpha = t$ and $t \in [-1, 1]$ it leads to

$$B(t) = \sum_{n=0}^{\infty} \frac{2n+1}{4\pi} B_n P_n(t) \quad (25)$$

which is the inverse Legendre transformation. Note that the convolution kernel only depends on the spherical distance between the two points \mathbf{x} and \mathbf{x}_p , thus, convolution kernels of this type are isotropic. For $\mathbf{x} = \mathbf{x}_p$, the spherical distance is zero and the kernel function reaches its maximum.

3.2 Filtering and representation in spherical radial basis functions

A (gravity) signal can be filtered by convolution with a kernel. The filter's spectral characteristic is defined by the coefficients B_n . For example, for $B_n = 0 \forall n > N$ and $B_n \neq 0 \forall n < N$, the convolution with the respective kernel results in a low-pass filtering. With the choice of the coefficients B_n , the convolution kernel can be adjusted according to the desired filtering effect. An example is the representation of a certain

signal bandwidth with a band-pass filter, while other frequency bands, which are of less interest, can be damped or discarded. Another interesting application of combining different filters is a multi resolution representation (MRR), see for example [Schmidt et al. \(2007\)](#) or [Gerhards \(2012\)](#). Kernels which cover different parts of the spectrum can be used to represent and combine observations in different bandwidths to one high resolution signal. This is very useful for the gravity signal, since different types of observations at different signal bandwidths, like spaceborne, airborne, or terrestrial, can be effectively combined.

To filter an observed gravity signal F with a kernel B , the convolution of the kernel with the signal, as derived in Eq. (22), reads:

$$G(\mathbf{x}) = (B * F)(\mathbf{x}) \approx \int_{\Omega_R} B(\mathbf{x}, \mathbf{x}_p) F(\mathbf{x}_p) d\omega, \quad (26)$$

where G is the filtered (gravity) signal. If B is the reproducing kernel from Eq. (20), $G = F$ holds. Again, one option to compute the filtered signal G is to evaluate the integral numerically.

Assume that the signal F and the kernel B are both member of the same space, a Hilbert space on the sphere, then the result of the convolution of the two functions $(B * F)$ is in the same space and can be represented in a linear combination of the kernel B .

$$(B * F)(\mathbf{x}) = \sum_{k=1}^{\infty} d_k B(\mathbf{x}, \mathbf{x}_k) \approx \sum_{k=1}^K d_k B(\mathbf{x}, \mathbf{x}_k) \quad (27)$$

The kernel B at different locations \mathbf{x}_k span the Hilbert space and d_k are coefficients to represent the signal in the kernel radial basis functions. A band-limited signal F can be exactly represented by a summation up to the function's maximum polynomial degree N .

3.3 Determination of the coefficients by parameter estimation

Instead of determining the fields, filtered by a kernel function, with a numerical evaluation of the convolution integral, as in Eq. (26), another approach is to determine the coefficients d_k in Eq. (27) by parameter estimation. Parameter estimation is a very common approach to different problems in geodesy, and it has a number of advantages to offer, in contrast to the method of numerical evaluation of the integrals. The main advantages are:

1. The possibility to combine different types of observations in one parameter estimation step. In the case of gravity observations these could be for example terrestrial, airborne and satellite data.
2. No grid interpolation of the data is needed as it is for numerical integration.
3. Accuracy assessment of the results is a part of the estimation step and different accuracies in the observations can be accounted for by error propagation. This

type of rigorous quality assessment is not possible in the numerical integration approach.

4. Up- and downward continuation of the observations is directly performed in the estimation step, with the factor $\left(\frac{R}{r}\right)^{n+1}$ in the kernel, see Eq. (23). In the case of gravity observations this means that, for example, from observations at satellite orbit height a gravity representation at a mean Earth surface can be directly computed. However downward continuation of a gravity signal is an ill-posed problem because of gravity attenuation with distance from the masses. Regularization methods are needed in order to solve the system and estimate values for the coefficients d_k , see Sect. 5.

Based on Eq. (27), an observed signal F can be modelled as:

$$F(\mathbf{x}) + e(\mathbf{x}) \approx \sum_{k=1}^K d_k B(\mathbf{x}, \mathbf{x}_k), \quad (28)$$

where $e(\mathbf{x})$ are the observational errors. Also high frequency signal patterns, higher than the maximum degree N of the kernel B cannot be modelled and are projected into the error vector. The number of grid points K is derived from the kernel.

4 Regional gravity field modelling in radial basis functions

Due to their localizing properties, radial basis functions are used for regional signal representations rather than global applications.

Spherical harmonics, which are global oscillating functions, are very appropriate to represent the long wavelength part of the gravity signal of the Earth. But if a more detailed gravity potential signal of the Earth has to be represented, it is advisable to use basis functions with local support for appropriate modelling of regional detailed signals. For basis functions on the sphere with local support, we only focus on radial basis functions. A very viable option in gravity field representation is to combine basis functions with global support and basis functions with local support. In this case, the gravity potential up to a certain degree N is represented in spherical harmonics, and local refinements, in terms of basis functions with local support, are added in order to model the residual signal ΔF .

$$F(\mathbf{x}) = \sum_{n=0}^N \sum_{m=-n}^n F_{nm} Y_{nm}(\mathbf{x}) + \Delta F(\mathbf{x}) \quad (29)$$

In the subsequent part of this article, we focus on the modelling of the regional residual gravity signal ΔF . When working with a regional signal, there are issues like boundary and edge effects to be considered, which do not occur in the global case. Regional gravity modelling introduces other difficulties than well-studied global modelling and shall therefore be investigated in detail.

Analogous to Eq. (27), a regional, residual, and band-limited gravity signal ΔF can be modelled as:

$$\Delta F(\mathbf{x}) + e(\mathbf{x}) = \sum_{k=1}^K d_k B(\mathbf{x}, \mathbf{x}_k). \quad (30)$$

The unknown coefficients d_k can be estimated via

$$\Delta \mathbf{F} + \mathbf{e} = \mathbf{A} \cdot \mathbf{d} \quad (31)$$

$$\begin{bmatrix} \Delta F_1(\mathbf{x}_1^1) \\ \vdots \\ \Delta F_1(\mathbf{x}_i^1) \\ \Delta F_2(\mathbf{x}_j^1) \\ \vdots \\ \Delta F_2(\mathbf{x}_L^1) \end{bmatrix} + \begin{bmatrix} e_1(\mathbf{x}_1^1) \\ \vdots \\ e_1(\mathbf{x}_i^1) \\ e_2(\mathbf{x}_j^1) \\ \vdots \\ e_2(\mathbf{x}_L^1) \end{bmatrix} = \begin{bmatrix} B_1(\mathbf{x}_1^1, \mathbf{x}_1) & \cdots & B_1(\mathbf{x}_1^1, \mathbf{x}_K) \\ \vdots & \ddots & \vdots \\ B_1(\mathbf{x}_i^1, \mathbf{x}_1) & \cdots & B_1(\mathbf{x}_i^1, \mathbf{x}_K) \\ B_2(\mathbf{x}_j^1, \mathbf{x}_1) & \cdots & B_2(\mathbf{x}_j^1, \mathbf{x}_K) \\ \vdots & \ddots & \vdots \\ B_2(\mathbf{x}_L^1, \mathbf{x}_1) & \cdots & B_2(\mathbf{x}_L^1, \mathbf{x}_K) \end{bmatrix} \cdot \begin{bmatrix} d_1 \\ \vdots \\ d_K \end{bmatrix}$$

Hereby, ΔF_1 and ΔF_2 , respectively e_1 , e_2 , B_1 , and B_2 indicate that two (or more) different types of observations can be used. In the case of gravity observations these could be for example satellite and terrestrial observations. Terrestrial observations cover much higher frequencies than space borne observations. The two different kernels, B_1 and B_2 , which could be used to take that fact into account, cover the respective bandwidths of the observations. That means in Eq. (23) the Legendre coefficients B_{n1} are zero outside the frequency band covered by observations F_1 , and respectively for the kernel coefficients B_{n2} .

If different functionals of the gravity potential are observed, only the kernel B needs to be adjusted accordingly. But the parameters d_k can still be estimated in one step.

5 Solution of the inverse problem

The system of equations to be solved in (31) is most likely a singular system. There are several reasons for singularities, and the main ones are:

1. Most likely, more basis functions B are used than minimally needed. In most cases the radial basis functions are located on a grid, and thus, the grid structure constrains the number of basis functions in use. Also, in numerical experiments we have seen that a slightly higher number of radial basis functions gives better modelling results than the minimal number which is theoretically required.
2. A lot of sets of observations have data gaps.
3. The downward continuation of airborne and spaceborne gravity observations is a singular problem by itself. Observations for modelling the gravity potential of the Earth would most likely involve airborne or spaceborne data, since with terrestrial measurements only a good temporal and spatial coverage is almost impossible.

We use and compare two different methods to handle the singularity of the system $\Delta \mathbf{F} + \mathbf{e} = \mathbf{A} \cdot \mathbf{d}$ with singular normal equation matrix $\mathbf{A}^T \mathbf{A}$. These are:

5.1 Truncated singular value decomposition

In this method, a truncated singular value decomposition is used to compute the pseudoinverse of the normal equation matrix $(\mathbf{A}^T \mathbf{A})^+$. The normal equation matrix is decomposed into $\mathbf{A}^T \mathbf{A} = \mathbf{U} \Sigma \mathbf{V}^T$, where Σ is a diagonal matrix with the singular values on the main diagonal, the columns of \mathbf{U} are the left singular vectors of $\mathbf{A}^T \mathbf{A}$ or the eigenvectors of $\mathbf{A}^T \mathbf{A} (\mathbf{A}^T \mathbf{A})^T$, and the columns of \mathbf{V} are the right singular vectors of $\mathbf{A}^T \mathbf{A}$ or the eigenvectors of $(\mathbf{A}^T \mathbf{A})^T \mathbf{A}^T \mathbf{A}$. Thus, $\mathbf{V} = \mathbf{U}$ holds. See for example [Press et al. \(2007\)](#). The pseudoinverse $(\mathbf{A}^T \mathbf{A})^+$ is computed via $(\mathbf{A}^T \mathbf{A})^+ = \mathbf{V} \Sigma^+ \mathbf{U}^T$. In the diagonal matrix Σ^+ all elements from Σ , which are larger than or equal to a given number, for which we choose 10^{-11} , are replaced by their reciprocal and all elements smaller than this number are replaced by zero.

The estimated coefficients $\hat{\mathbf{d}}$ are determined by

$$\hat{\mathbf{d}} = (\mathbf{A}^T \mathbf{A})^+ \mathbf{A}^T \Delta \mathbf{F}. \quad (32)$$

5.2 With prior information

With the help of prior information about the coefficients \mathbf{d} , regularization of the singular system can be performed. Additional information with the expectation vector $\boldsymbol{\mu} = E(\mathbf{d})$ and its covariance matrix $D(\mathbf{d}) = \mathbf{P}_{\boldsymbol{\mu}}^{-1}$ is used and the weight between the a priori information and the observations is determined by the regularization parameter λ . The coefficients $\hat{\mathbf{d}}$ and are to be estimated and are according to [Koch and Kusche \(2002\)](#) determined by

$$\hat{\mathbf{d}} = (\mathbf{A}^T \mathbf{A} + \lambda \mathbf{P}_{\boldsymbol{\mu}})^{-1} (\mathbf{A}^T \Delta \mathbf{F} + \lambda \mathbf{P}_{\boldsymbol{\mu}} \boldsymbol{\mu}). \quad (33)$$

[Koch and Kusche \(2002\)](#) propose variance component estimation to determine the regularization parameter λ . With this method, the unknown variance components of the observations (σ^2) and of the expectation vector ($\sigma_{\boldsymbol{\mu}}^2$) are estimated iteratively, and the regularization parameter λ is determined by $\lambda = \hat{\sigma}^2 / \hat{\sigma}_{\boldsymbol{\mu}}^2$. We use this approach for our example with noise on the observations. Since a residual gravity signal is modelled, we set the prior values of the coefficients in vector $\boldsymbol{\mu}$ to zero, and use an identity matrix for its covariance matrix. For the noise-free case we choose the regularization parameter λ to be 10^{-8} .

6 Numerical simulation for different radial basis functions

6.1 Definition of the functions

In order to investigate different types of radial basis functions for regional gravity modelling, a given regional residual gravity signal from spherical harmonic degrees 150 to 250 in the Himalayan area is represented in the different radial basis functions in question. Thereby, we use the same number of basis functions, the same grid point spacing, the same area, and the same margin widths, which will all be explained in

more detail in Sect. 6.2, for all the functions. This allows for a direct comparison of their performance. The signal bandwidth corresponds to the sensitive bandwidth in GOCE satellite gravity measurements. The radial basis functions B which we use can all be represented by

$$B(\mathbf{x}, \mathbf{x}_k) = \sum_{n=0}^{\infty} \frac{2n+1}{4\pi} B_n P_n(\mathbf{r}^T \mathbf{r}_k), \quad (34)$$

which was derived in Eq. (24), and are defined by the coefficients B_n . Figure 1 shows the radial basis functions we use in spatial and frequency domains, and their definitions are given in the following. The functions are normalized, and to improve their inter-comparability the Shannon band-pass kernel is plotted again along with each other of the radial basis functions under consideration.

6.1.1 Shannon low-pass function

The Shannon low-pass function, see Eq. (35), is probably the most simple radial basis function. All coefficients up to a certain degree N are equal to one and all above N are zero. However, this sharp drop in the frequency domain causes strong oscillations in the spatial domain. We choose $N = 250$, which corresponds to the maximum degree in the signal bandwidth.

$$B_n = 1 \quad \forall \quad n \in [0, N]. \quad (35)$$

6.1.2 Shannon band-pass function

The Shannon band-pass function, as given by its coefficients in Eq. (36), covers exactly the bandwidth of our example signal (degrees 150–250), with our choice of the parameters $n_1 = 150$ and $n_2 = 250$. Due to this exact match, no other frequencies than the actual signal can be modelled. In the spatial domain, the first side lobe of the oscillations is even higher than for the Shannon low-pass function. Theoretically, radial basis functions are global functions, but, due to their localizing property, the influence of areas far from the center is very small. When radial basis functions are used for regional modelling, as in our examples here, this influence outside the area of consideration is neglected. Strong oscillations, as they occur here for the Shannon band-pass kernel, have therefore a negative effect on the regional modelling result.

$$B_n = \begin{cases} 1 & \forall \quad n \in [n_1, n_2] \\ 0 & \text{else.} \end{cases} \quad (36)$$

6.1.3 Blackman low-pass function

The Blackman low-pass function, see Eq. (37), has in contrast to the Shannon low-pass function presented in Sect. 6.1.1 a smoother drop in the frequency domain. The smooth transition from coefficients of value one to coefficients of zero in the frequency domain

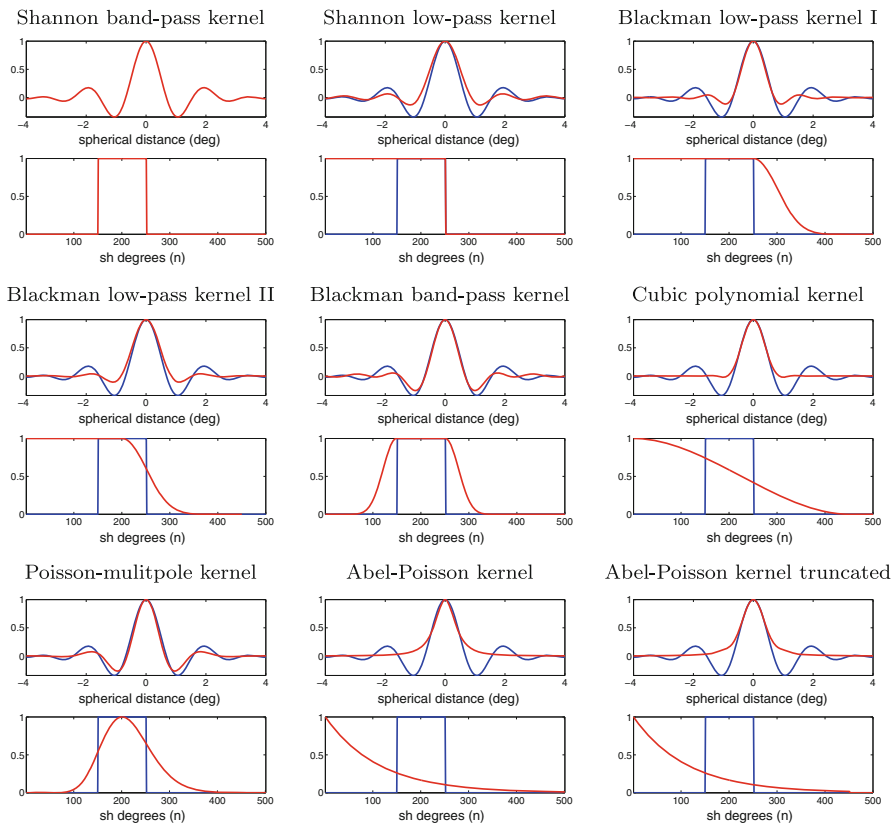


Fig. 1 Plots in the spatial and frequency domain of all kernels under consideration. The Shannon band-pass kernel is repeated in all figures to make comparisons easier (it covers exactly the bandwidth of the signal)

reduces the oscillations in the spatial domain significantly. We study two different scenarios of Blackman low-pass functions, which are derived from different values for the parameters n_1 and n_2 in Eq. (37). We use the parameter values $n_1 = 250$ and $n_2 = 450$ for type I, and $n_1 = 200$ and $n_2 = 400$ for type II. While in the case of Blackman low-pass function type I significantly higher frequencies are modelled than actually included in the signal (up to degree 250), in the case of Blackman scaling function type II a part of the signal spectrum cannot be modelled. This leads to omission errors in the regional modelling result. Both functions are plotted in Fig. 1.

$$B_n = \begin{cases} 1 & \text{for } n < n_1 \\ (A(n))^2 & \text{for } n = n_1, \dots, n_2 \\ 0 & \text{for } n > n_2 \end{cases} \quad (37)$$

$$A(n) = \frac{21}{50} - \frac{1}{2} \cos\left(\frac{2\pi(n - n_1)}{2(n_2 - n_1)}\right) + \frac{2}{25} \cos\left(\frac{4\pi(n - n_1)}{2(n_2 - n_1)}\right).$$

6.1.4 Modified Blackman band-pass function

A regular Blackman wavelet function is constructed as the difference between two Blackman scaling functions of two subsequent levels. Thus, it has a clear peak in the frequency domain with only one point equal to one. In contrast to the Blackman wavelet, we allow our modified Blackman band-pass function to have a flat top, see Eq. (38) and the graph in Fig. 1. Thus, the modified Blackman band-pass function fits better to the signal bandwidth in the frequency domain than a regular Blackman wavelet, while still maintaining the benefits of a Blackman band-pass function in contrast to the Shannon band-pass function. These are the smooth transition from value zero to one and back instead of the sharp drop and therefore less oscillations in the spatial domain. Note that our goal here is to optimally model our example signal which has a bandwidth of degrees 150–250. That is why our modification is useful here. n_1 and n_2 define the width of the flat top, n_{p1} and n_{p2} define the width of the transition for the sinusoidal drop to both sides of the flat top. We use $n_1 = 150$, $n_2 = 250$, $n_{p1} = n_{p2} = 110$. If the band-pass function is used to model a detail signal, as the difference between two levels, the regular wavelet-version, as given for example in Schmidt et al. (2007), is more appropriate to use.

$$B_n = \begin{cases} 0 & \text{for } n < n_1 - n_{p1} \\ 1 - (A_{n_{p1}}(n))^2 & \text{for } n \in [n_1 - n_{p1}, n_1] \\ 1 & \text{for } n = n_1 + 1, \dots, n_2 - 1 \\ (A_{n_{p2}}(n))^2 & \text{for } n \in [n_2, n_2 + n_{p2}] \\ 0 & \text{for } n > n_2 + n_{p2} \end{cases} \quad (38)$$

$$A_{n_{p1}}(n) = \frac{21}{50} - \frac{1}{2} \cos\left(\frac{2\pi(n - (n_1 - n_{p1}))}{2n_{p1}}\right) + \frac{2}{25} \cos\left(\frac{4\pi(n - (n_1 - n_{p1}))}{2n_{p1}}\right)$$

$$A_{n_{p2}}(n) = \frac{21}{50} - \frac{1}{2} \cos\left(\frac{2\pi(n - n_2)}{2n_{p2}}\right) + \frac{2}{25} \cos\left(\frac{4\pi(n - n_2)}{2n_{p2}}\right).$$

6.1.5 Cubic polynomial kernel

Another kernel with fairly small side-lobes in the spatial domain is the cubic polynomial kernel. The coefficients, which specify the kernel in the frequency domain, are given through a cubic polynomial, which goes from one for degree zero to zero for the maximum degree. Additionally, the polynomial's tangents in the frequency domain are horizontal for degree zero and the maximum degree which we choose at $n_{\max} = 450$. That gives a very smooth transition. The definition of the kernel is given in Eq. (39), and for an illustration see Fig. 1.

$$B_n = \left(1 - \frac{1}{n_{\max}} n\right)^2 \left(\frac{2}{n_{\max}} n + 1\right). \quad (39)$$

6.1.6 Poisson multipole kernel

The Poisson multipole kernel (Eq. 40) has first been introduced by [Holschneider et al. \(2003\)](#), but is, for example, also presented in [Chambodut et al. \(2005\)](#) and [Panet et al. \(2005\)](#). They state that the Poisson multipole kernel is of special interest for gravity field modelling because the shape may be identified with the potential from a multipole source. They call the parameter a the shape parameter and state that it is linked to the depth of the multipole in case of a unit sphere by $\|\mathbf{e}\| = e^{-a}$. \mathbf{e} is the position vector of the multipole, l is the order of the multipole; a large l improves the frequency localization, but simultaneously deteriorates the spatial localization. Additionally, [Panet et al. \(2010\)](#) give an example of using a Poisson multipole wavelet frame for gravity modelling over Japan.

In our example, we do not follow their interpretation of the parameters a and l , but we choose the two parameters such that the turning points in curvature of the kernel's expression in the frequency domain coincide with the bandwidth of our example signal. That is, we compute a and l from $\frac{d^2 B_n}{dn^2} = 0$ for $n = 150$ and $n = 250$ and obtain $l = 16$ and $a = 32/400$. Figure 1 gives an illustration of the kernel.

$$B_n = (an)^l e^{-an}. \quad (40)$$

6.1.7 Abel-Poisson kernel

The Abel-Poisson kernel is a non-band-limited kernel, and the only non-bandlimited radial basis function in our considerations. It can be represented in the same way as the other kernels under consideration in a Legendre expansion, but its analytical expression allows evaluation of the summation up to infinity, see Eq. 41. The parameter p , with $p = 0.009$, is chosen such that the width of the peak in the spatial domain is similar to the peaks in the spatial domain of the other kernel functions used here, since we want to use the same grid point spacing for all kernels. However, in order to provide an appropriate grid spacing for the non-band-limited Abel-Poisson kernel, the number of grid points should be infinite, since the kernel contains frequencies up to infinity. Of course, this is numerically not possible. Therefore, we also use a truncated version of the Abel-Poisson kernel, see the following Sect. 6.1.8.

A plot of the Abel-Poisson kernel in spatial and frequency domain is given in Fig. 1. In contrast to the radial basis functions presented so far, the Abel-Poisson kernel does not have negative values in the spatial domain, it does not show the oscillations which we have seen for the other radial basis functions. In the spatial domain, it is the smoothest of our functions under consideration, and therefore, has the best spatial localizing properties. Also, the behaviour in the frequency domain is very different to what we have seen for the radial basis functions presented before. The spectrum covered is not adapted to the signal bandwidth.

$$\sum_{n=0}^{\infty} \frac{2n+1}{4\pi} h^n P_n(r^T r_k) = \frac{1}{4\pi} \frac{1-h^2}{(1-2ht+h^2)^{3/2}} \quad (41)$$

$$B_n = h^n, \quad h = e^{-p}, \quad t = \cos(\psi) = \cos(r^T r_k).$$

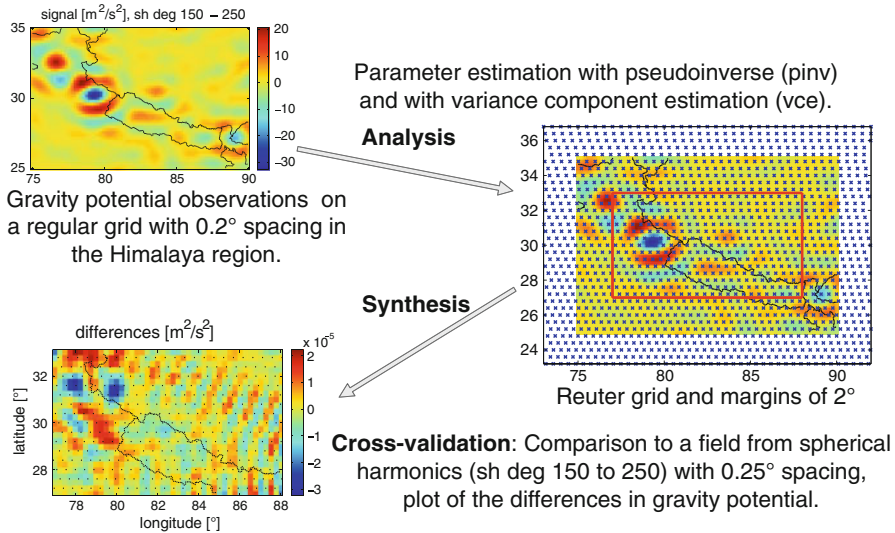


Fig. 2 Illustration of the numerical simulation

6.1.8 Truncated Abel-Poisson kernel

As already mentioned in the descriptions of the non-truncated Abel-Poisson kernel, Sect. 6.1.7, we also want to investigate a truncated, and therefore band-limited, version of the Abel-Poisson kernel. The equations of the kernel are given in Eq. (42), and we use the same value for the parameter p as in the non-truncated case. Furthermore, we use $N = 450$ as cut-off degree. Its behaviour in the spatial domain is very similar to the non-band-limited Abel-Poisson kernel, and in the frequency domain both kernels share exactly the same behaviour up to the cut-off frequency.

$$B_n = h^n, \quad h = \begin{cases} e^{-p} & \text{for } n \leq N \\ 0 & \text{for } n > N. \end{cases} \quad (42)$$

6.2 Rationale of the simulation

The first step in the simulation is the creation of simulated observations. A residual gravity potential is obtained by using the difference signal from the geopotential models EGM2008 and EGM96 within the spherical harmonic degrees 150–250. The observations of this residual gravity potential are constructed on a regular grid in the Himalayan area with 0.2° grid spacing, see Fig. 2. The Himalayan area is chosen, for the reason that this area has a very strong signal in the geopotential models. That provides more of a challenge to the modelling in terms of boundary and ringing effects.

In a second step, these observations are analyzed by representing the signal in radial basis functions according to the linear model given in Eqs. (30) and (31). The radial basis functions are placed on a Reuter grid, see (Freeden et al. 1998, p. 171). Thereby, the global number of grid points, respectively the point density, is determined

by the parameter γ , with $\Delta\vartheta = \frac{\pi}{\gamma}$, where $\Delta\vartheta$ is the spacing of the grid points along the meridians. We choose $\gamma = 450$ for all different radial basis functions in our simulations in order to obtain comparable results. The value for γ is derived from the maximum degree in the kernel, and, thus, also from the width of the peak in the spatial domain. All parameters in the kernels in our simulations are chosen such that the kernels fit to a grid spacing with $\gamma = 450$.

Finally, the third step is a cross-validation of the results. Therefore, the regional field in question is synthesized on an independent regular grid with 0.25° spacing by the series expansions from both the newly estimated coefficients of the radial basis functions and the original spherical harmonic coefficients. The two synthesized fields are compared by evaluation of their differences in each point to determine the error of the regional gravity field representation. Error residual grids are obtained from the differences for each of the derived regional representations. For each of these residual grids, a root mean square (RMS) value is computed as a measure for the quality of the regional representation. A corresponding relative quality measure is derived by dividing each error RMS by the RMS of the original signal evaluated at the same grid points. In the following, this value is called relative RMS and used to evaluate and compare the performance of the different radial basis functions in regional gravity modelling.

Furthermore, the inverse problem of estimating the coefficients for the regional representation is solved by the two different methods explained in Sects. 5.1 and 5.2, which are compared to each other as well. The estimated coefficients might fulfill the equations, but are not necessarily physically meaningful values. The inverse problem in our case has an unlimited number of solutions. To take into account that we are interested in finding physically meaningful solutions, we also compute correlation coefficients between the values of the estimated coefficients \mathbf{d} and the signal computed at the respective points directly from spherical harmonics. In a meaningful solution the estimated coefficients are highly correlated with the signal.

Figure 2 gives an illustration of the numerical simulation steps. The plot on the right hand side shows the Reuter grid, where the radial basis functions are located, along with the observations. In order to avoid boundary effects at the edge of the area, we add observations in a 2° margin around the area of investigation and an additional 2° margin for the grid points where additional radial basis functions are placed. Observations in our simulation cover the area from 75° to 90° longitude and 25° to 35° latitude. This leads to a system with 3,876 observations which are used to determine 1,437 unknowns. 1,125 points are used in the cross-validation.

The simulation is run for each of the different radial basis functions described in Sect. 6.1 and both of the methods to solve the singular system (Sects. 5.1 and 5.2). First, the observations are treated as noise-free. Then, in a second run, all scenarios are repeated with white noise in the order of $0.1 \text{ m}^2/\text{s}^2$ added to the observations. This error level corresponds to the expected accuracy of the gravity potential on the sphere derived from GOCE observations.

6.3 Comparison of the simulation results for the different kernels

Table 1 lists the results of the simulation for all of the different kernels and both estimation methods, truncated singular value decomposition and with prior information.

Table 1 Summary of results from **noise-free** data using all different kernels and both estimation methods, truncated singular value decomposition (SVD) and prior information (prior info); columns two and three give the relative error, as the percentage of the error RMS of the signal RMS, and columns four and five contain the correlation coefficients between the estimated coefficients and the signal

	Relative error		Correlation coefficient	
	svd (%)	Prior info (%)	svd	Prior info
Shannon kernel (low pass)	1.2e−3	2.7e−3	0.032	0.25
Shannon kernel (band-pass)	2.5e−3	7.3e−3	0.0024	0.029
Blackman low-pass type I	6.1e−4	7.6e−5	0.89	0.92
Blackman low-pass type II	1.1e−3	1.5e−4	0.68	0.87
Mod. Blackman band-pass	1.3e−3	3.8e−4	0.36	0.69
Cubic polynomial kernel	5.8e−4	6.7e−5	0.89	0.91
Poisson multipole kernel	4.2e−4	6.9e−5	0.72	0.85
Abel-Poisson kernel truncated	3.8e−4	9.1e−5	0.88	0.91
Abel-Poisson kernel	1.03	1.03	9.4e−4	0.050

The second and third column give relative RMS values of the errors and the signal and the last two columns give the correlation between the estimated coefficients and the signal. The relative RMS value gives an indication of the average magnitude of the representation error and the correlations indicate if the estimated coefficients are physically meaningful. We consider a solution meaningful, if the coefficients reflect the signal to a large extent. In a solution which only represents the input signal in the mathematical sense, the coefficients can have values which do not resemble the signal structure, these can be for example very large values in the margins and small values in the area of interest. Even though these solutions might represent the signal very well, only physically meaningful coefficients can be used for filtering, signal decomposition, transformation between different gravity field functionals, up- and downward continuation, or data compression. The correlation can also be seen in the graphical representations of the coefficients of which some examples are given in the next subsection.

Comparing all band-limited kernels, the errors from the Shannon kernels are higher than the errors from the other kernels. This is most likely due to the strong oscillations which occur in the spatial domain and clearly demonstrates the importance of a good spatial localization of the kernels. However, even though the Poisson multipole kernel has a fairly low first minimum and high first maximum in the spatial domain, compared to the other kernels under consideration, its oscillations flatten out quickly with distance from its center. This is not the case for the oscillations of the Shannon kernels. Since the kernels are global functions, with quasi-localizing properties, strong oscillations outside the area of interest lead to leakage and a bad regional modelling result. Low errors are obtained from the Blackman low-pass kernel type I, the cubic polynomial kernel, the Poisson multipole kernel, and the truncated Abel-Poisson kernel. The fixed Reuter grid parameter, which we use for comparability of the results, is with $\gamma = 450$ fairly low for the non-band limited Abel-Poisson kernel. This is the reason for the high errors with this kernel.

For the Blackman low-pass kernel type I, the cubic polynomial kernel, and the truncated Abel-Poisson kernel the correlation between the estimated coefficients and the signal are also very high, with correlation coefficients of slightly above 0.9 for the results with prior information and slightly below 0.9 for the results from the truncated singular values decomposition. Thus, we consider these three kernels as the best options for regional gravity signal representation. Even though the errors are small for the Poisson multipole kernel as well, the correlations of the coefficients with the signal are slightly lower than for the three other kernels.

In a next step, all simulation scenarios are repeated but with white noise added to the observations. The standard deviation of the white noise is chosen to be $0.1 \text{ m}^2/\text{s}^2$ which corresponds to 1 cm geoid error and is roughly the expected noise level of geoid heights derived from the GOCE gravity mission. In Table 2 the results from the simulations with noise on the observations are listed.

In all cases of band-limited kernels the relative errors increase about three orders of magnitude compared to the noise free case. Only for the non-band limited Abel-Poisson kernel the results are not significantly worse with 1.06 % relative error compared to 1.03 % in the noise free case. The regularization with variance component estimation leads to slightly better results than the truncated singular value decomposition. While the errors from both methods are in the same order of magnitude, there is a big difference between the correlations between the estimated coefficients and the signal in the solutions from the two different methods. The results obtained with singular value decomposition do not show any correlation with the signal, the correlations are not higher than 1.5 % for all of the different kernels. Thus, we conclude that in the presence of noise, only prior information (with variance component estimation) is capable to give the physically meaningful results we want to obtain.

Considering only the solutions derived with variance component estimation, we see that all kernels, besides the two Shannon kernels, lead to high correlations of about

Table 2 Summary of results from data with **white noise** in the order of $0.1 \text{ m}^2/\text{s}^2$ using all different kernels and both estimation methods, truncated singular value decomposition (SVD) and prior information (prior info); columns two and three give the relative error, as the percentage of the error RMS of the signal RMS, and columns four and five contain the correlation coefficients between the estimated coefficients and the signal

	Relative error		Correlation coefficient	
	svd (%)	Prior info (%)	svd	Prior info
Shannon kernel (low pass)	0.17	0.16	0.0097	0.76
Shannon kernel (band-pass)	0.16	0.20	0.015	0.40
Blackman low-pass type I	0.25	0.21	0.0074	0.92
Blackman low-pass type II	0.23	0.19	0.0072	0.89
Mod. Blackman band-pass	0.21	0.17	0.015	0.89
Cubic polynomial kernel	0.26	0.23	0.0040	0.92
Poisson multipole kernel	0.27	0.21	0.0036	0.87
Abel-Poisson kernel truncated	0.25	0.23	0.0030	0.92
Abel-Poisson kernel	1.06	1.06	0.00084	0.93

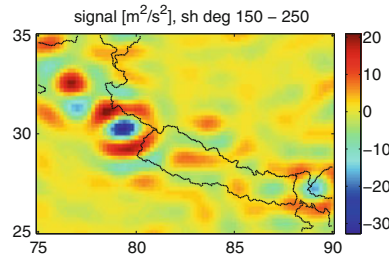


Fig. 3 Regional residual gravitational potential signal (in m^2/s^2) to be modelled

90 %. The non-band limited Abel-Poisson kernel shows the highest correlation (93 %) but leads to the largest relative errors (1 %). Taking a closer look at the other kernels, there are only marginal differences between the results. However, some systematics can be found. The first group comprises the truncated Abel-Poisson, the cubic polynomial and the Blackman low-pass type I kernels. They show high correlations of 92 %, and lead to relative errors of 0.21–0.23 %. The second group, with the Blackman low-pass type II, Blackman band-pass, and also the Shannon low-pass, and Poisson multipole kernels, have smaller errors of 0.16–0.21 %, but have also less correlated coefficients with 76–89 % correlation. This can probably be explained by the fact that the spectrum of the second group of kernels is more limited, and thus, they filter out more noise than the kernels in the first group, which have a wider spectrum and allow for more noise in the modelling result. The kernels of the first group are smoother in the spatial domain than the kernels of the second group and therefore offer better spatial localization. This explains the higher correlation of the estimated coefficients with the signal.

6.4 Examples of residuals and estimated coefficients from different kernels

In the following, graphical representations of residuals, estimated coefficients, their standard deviations, and their significance are given for selected kernels, from both parameter estimation methods, as well as for the noise-free and noise-contaminated observations. For comparison, the signal to be modelled is shown in Fig. 3. The estimated standard deviation $\hat{\sigma}_{d_k}$ of an estimated coefficient \hat{d}_k of the vector $\hat{\mathbf{d}}$ is derived from the covariance matrix of the estimated coefficients, which can be found in Eq. (14), given as

$$\hat{\sigma}_0^2 \mathbf{Q} = \hat{\sigma}_0^2 \begin{bmatrix} q_{11} & \cdots & q_{1K} \\ \vdots & & \vdots \\ q_{K1} & \cdots & q_{KK} \end{bmatrix} \quad (43)$$

$$\hat{\sigma}_{d_k} = \sqrt{\hat{\sigma}_0^2 q_{kk}}.$$

The simplified test statistic $|\hat{d}_k|/\hat{\sigma}_{d_k}$ is computed in order to have a measure if the individual coefficient \hat{d}_k is significantly different from zero. The significance of the

individual parameters can be checked with a t -test, thereby the hypothesis statements to test an individual coefficient d_k are:

$$\begin{aligned} H_0 : d_k &= 0 \\ H_1 : d_k &\neq 0 \end{aligned} \quad (44)$$

It holds the probability relation $P\{d_k < t_{f,1-\alpha} \mid H_{0k}\} = 1 - \alpha$. The null hypothesis H_0 would be accepted, if the test statistic $|d|/\sigma_d$ is smaller than the critical value for the t -test, which is

$$t_{L-K,1-\alpha} = t_{2439,0.99} = 2.33 \quad (45)$$

for $\alpha = 0.01$.

Figures 4, 5, and 6 show results from noise-free data, and Figs. 7, 8, and 9 show results from data with white noise. The plots of the residuals (in the first rows in each of the figures) show resonance structures in the solutions from prior information while the structures of the residuals in the solutions from the truncated singular value decomposition seem to be random. The second row in each of the figures shows the values of the estimated coefficients for both parameter estimation methods. We expect the estimated coefficients to resemble the signal, see Fig. 3. This correlation is also represented by the correlation coefficients given in Tables 1 and 2. We expect the standard deviation of the coefficients to be small in the inner area, while the margins are used to avoid edge effects around the area of observations. The estimated coefficients are supposed to decrease to zero outside the area of interest. The test statistic $|d|/\hat{\sigma}_d$ shows the significance of each of the estimated parameters. A value smaller than the critical value from the t -test (which is 2.33, see Eq. 45) means that this coefficient is not significant in the representation of the signal. We expect the coefficients in the inner area to be significant, while we expect the coefficients in the margin not to contribute significantly to the representation, i.e. not to be significantly different from zero.

While for the Shannon low-pass kernel (Fig. 4) no physically meaningful coefficients \mathbf{d} can be estimated, for the Blackman low-pass type I (Fig. 5) and for the truncated Abel-Poisson kernel (Fig. 6) the estimated coefficients \mathbf{d} resemble the signal in both cases, estimated via truncated singular value decomposition and with prior information. Also the standard deviations and the significance of the estimated coefficients for these two kernels show what we expect, in contrast to the Shannon low-pass kernel. The coefficients in the margins are, as expected, less significant than those over areas with a high signal energy, see Figs. 5 and 6.

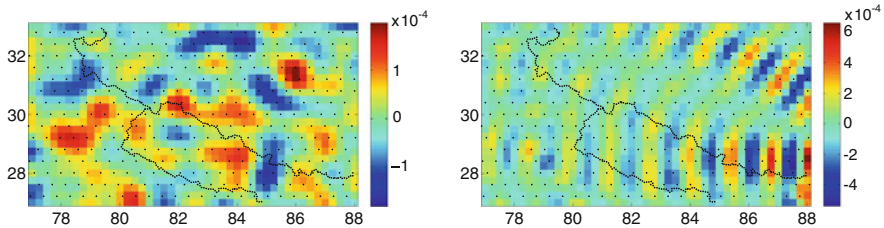
In the scenario with noise on the observations, it can be clearly seen from the values of the coefficients \mathbf{d} that the solutions obtained via a singular value decomposition are not reasonable for all the examples, see Figs. 7, 8, and 9. The values as well as their standard deviation are unreasonable high and do not at all resemble the signal structure as the coefficients \mathbf{d} do which were obtained via variance component estimation. Furthermore, for the Shannon low-pass (Fig. 7) and the cubic polynomial kernels (Fig. 8), most of the estimated coefficients from truncated singular value decomposition are not significantly different from zero, and for all the others the test statistics is very close to the critical value. Since the method of variance component estimation is designed

Shannon low-pass kernel

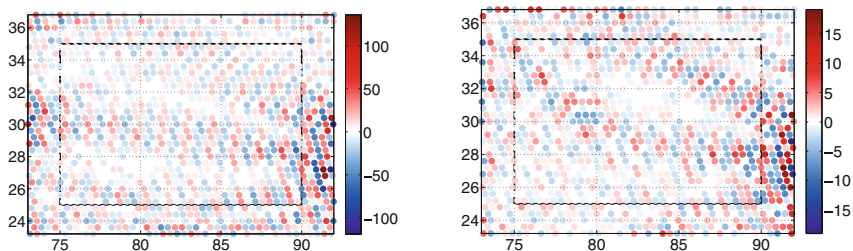
truncated singular values decomposition

prior information

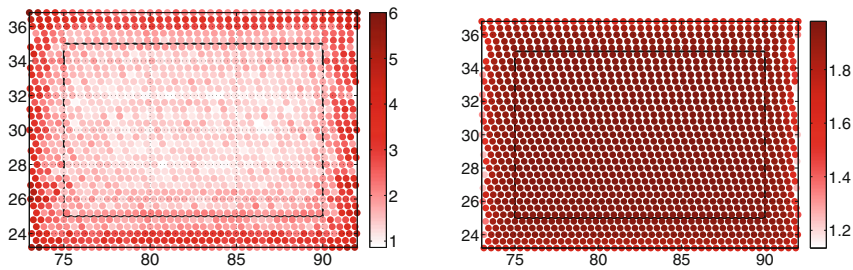
errors in the estimated fields [m^2/s^2]



values of the estimated coefficients d



standard deviation σ_d of the estimated coefficients



test statistic $|d|/\sigma_d$ of the estimated coefficients

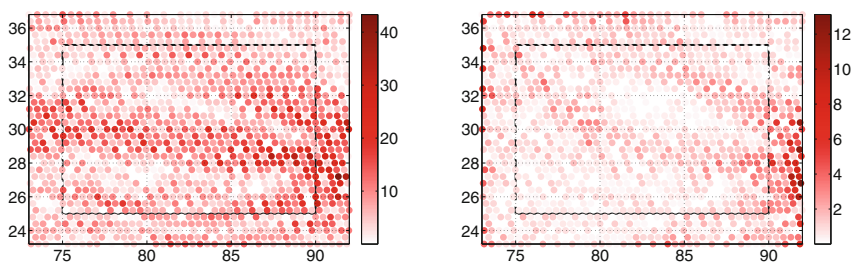


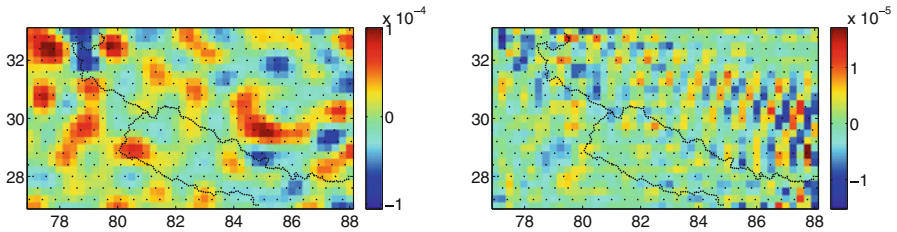
Fig. 4 Results from simulations with noise-free observations and the Shannon low-pass kernel: residuals in m^2/s^2 , values of the estimated coefficients \hat{d} , their estimated standard deviation $\hat{\sigma}_d$, and their significance $|\hat{d}|/\hat{\sigma}_d$ derived with truncated singular value decomposition (column on the left) and prior information (column on the right)

Blackman low-pass type I kernel

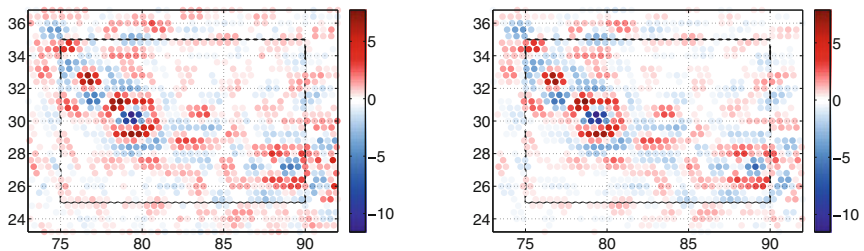
truncated singular values decomposition

prior information

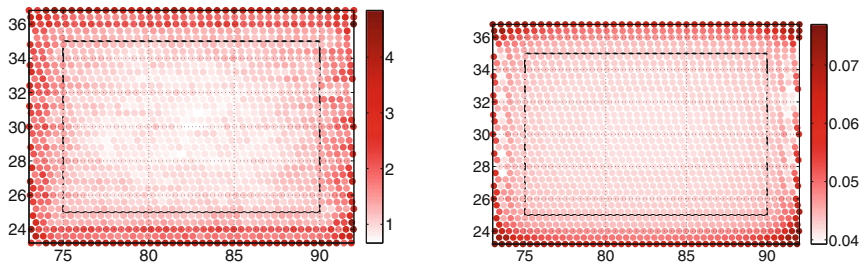
errors in the estimated fields [m^2/s^2]



values of the estimated coefficients d



standard deviation σ_d of the estimated coefficients



test statistic $|d|/\sigma_d$ of the estimated coefficients

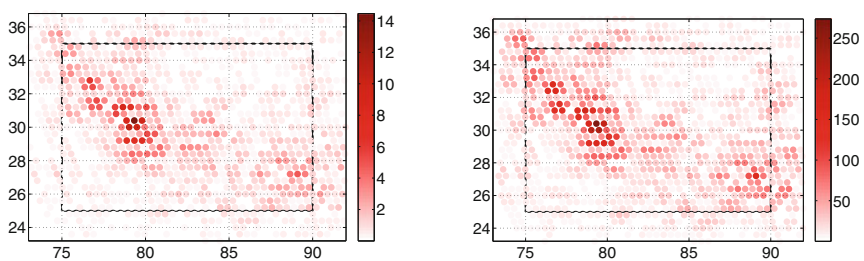


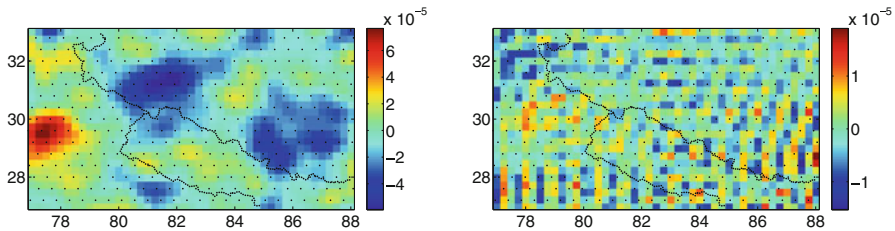
Fig. 5 Results from simulations with noise-free observations and the Blackman low pass type I kernel: residuals in m^2/s^2 , values of the estimated coefficients \hat{d} , their standard deviation $\hat{\sigma}_d$, and their significance $|\hat{d}|/\hat{\sigma}_d$ derived with truncated singular value decomposition (column on the left) and prior information (column on the right)

Truncated Abel-Poisson kernel

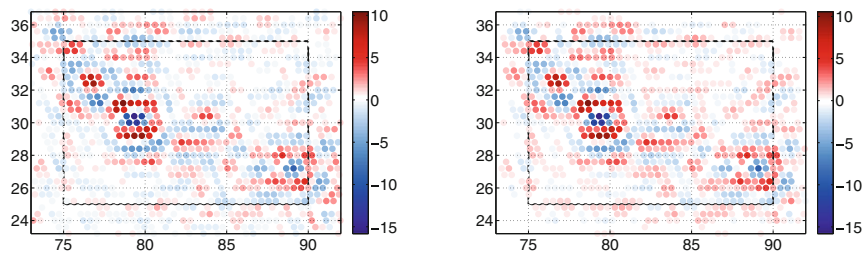
truncated singular values decomposition

prior information

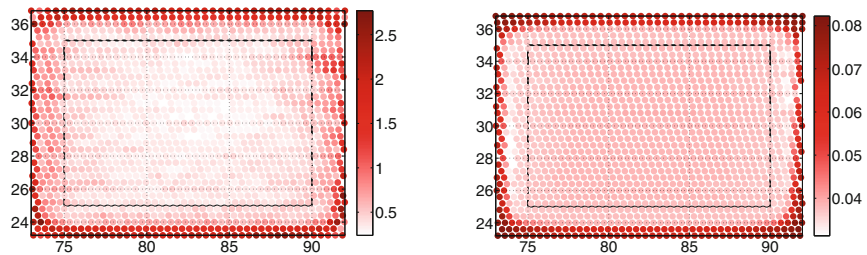
errors in the estimated fields [m^2/s^2]



values of the estimated coefficients \hat{d}



standard deviation $\sigma_{\hat{d}}$ of the estimated coefficients



test statistic $|\hat{d}|/\sigma_{\hat{d}}$ of the estimated coefficients

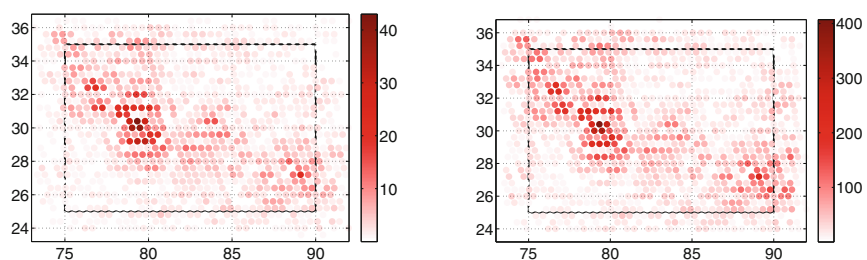
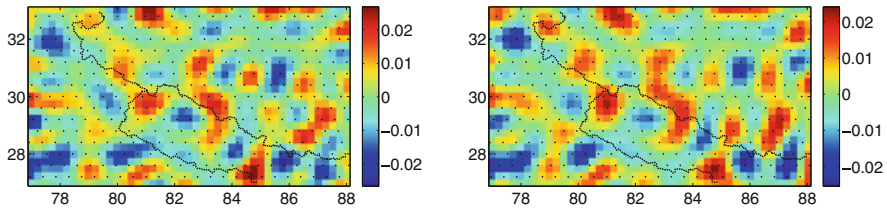


Fig. 6 Results from simulations with noise-free observations and the truncated Abel-Poisson kernel: residuals in m^2/s^2 , values of the estimated coefficients \hat{d} , their standard deviation $\hat{\sigma}_d$, and their significance $|\hat{d}|/\hat{\sigma}_d$ derived with truncated singular value decomposition (column on the left) and prior information (column on the right)

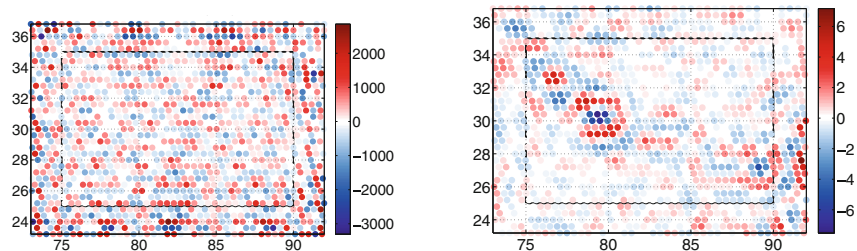
Shannon low-pass kernel, white noise on the observations

truncated singular values decomposition prior information

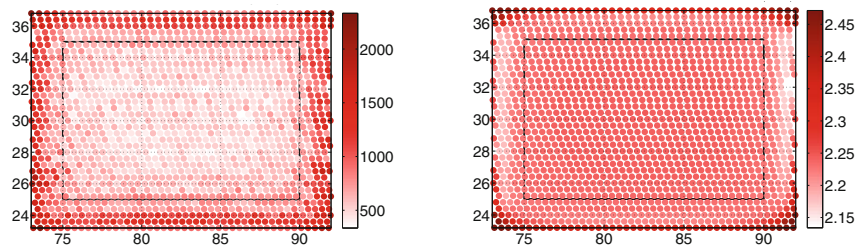
errors in the estimated fields [m^2/s^2]



values of the estimated coefficients d



standard deviation σ_d of the estimated coefficients



test statistic $|\hat{d}|/\sigma_d$ of the estimated coefficients

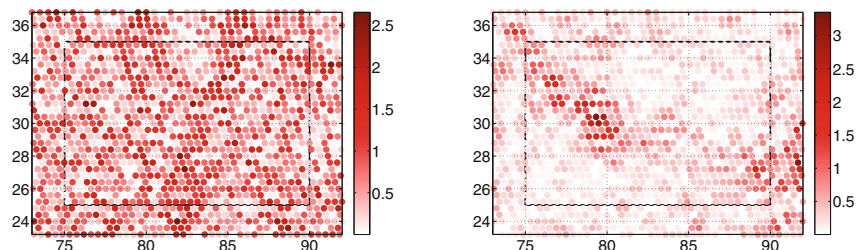


Fig. 7 Results from simulations with white noise added to the observations and the Shannon low-pass kernel: residuals in m^2/s^2 , values of the estimated coefficients \hat{d} , their standard deviation $\hat{\sigma}_d$, and their significance $|\hat{d}|/\hat{\sigma}_d$ derived with truncated singular value decomposition (*column on the left*) and prior information (*column on the right*)

Cubic polynomial kernel, white noise on the observations

truncated singular values decomposition

prior information

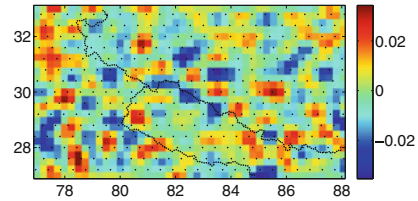
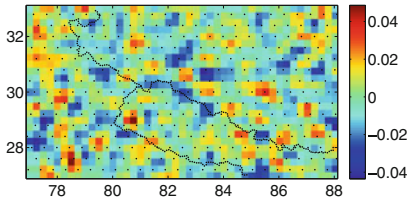
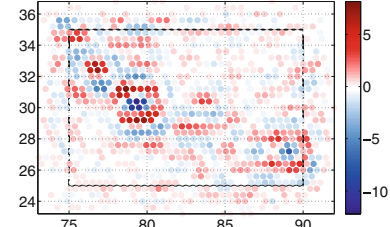
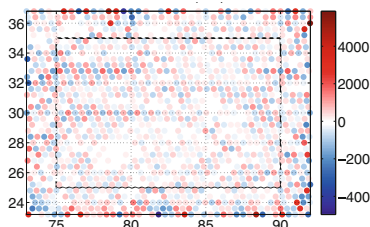
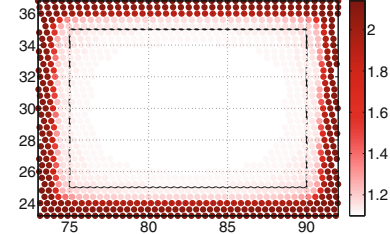
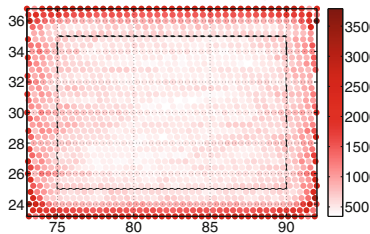
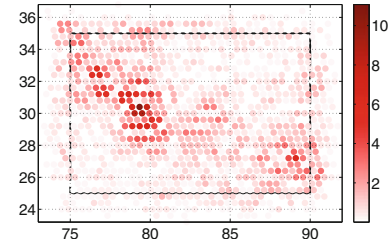
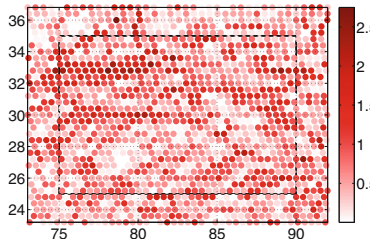
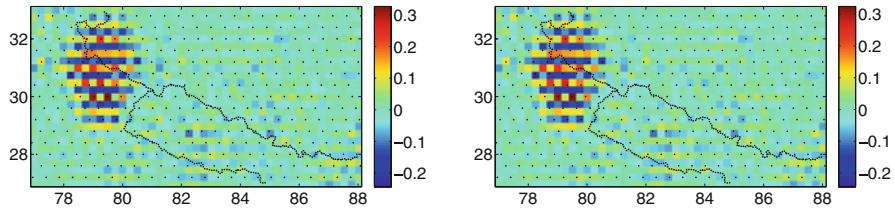
errors in the estimated fields [m^2/s^2]values of the estimated coefficients \hat{d} standard deviation σ_d of the estimated coefficientstest statistic $|\hat{d}|/\hat{\sigma}_d$ of the estimated coefficients

Fig. 8 Results from simulations with white noise added to the observations and the cubic polynomial kernel: residuals in m^2/s^2 , values of the estimated coefficients \hat{d} , their standard deviation $\hat{\sigma}_d$, and their significance $|\hat{d}|/\hat{\sigma}_d$ derived with truncated singular value decomposition (column on the left) and prior information (column on the right)

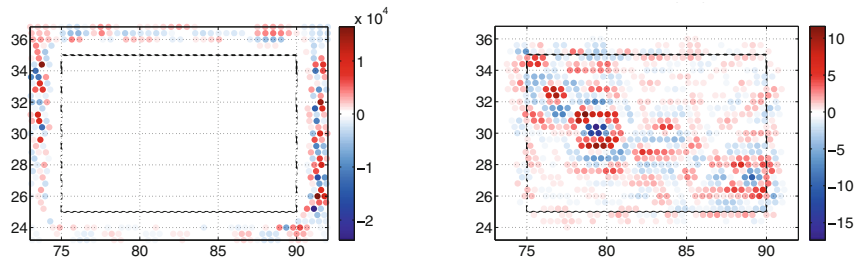
Abel-Poisson kernel, white noise on the observations

truncated singular values decomposition prior information

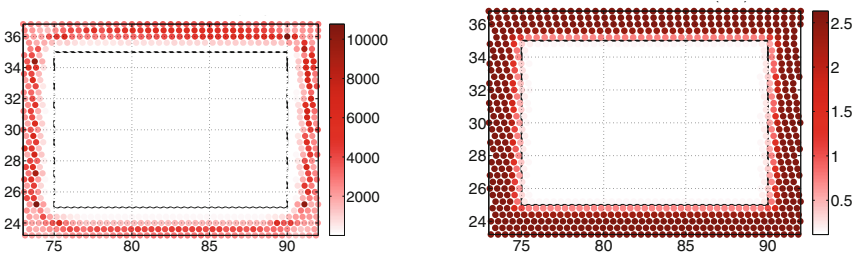
errors in the estimated fields [m^2/s^2]



values of the estimated coefficients d



standard deviation σ_d of the estimated coefficients



test statistic $|d|/\sigma_d$ of the estimated coefficients

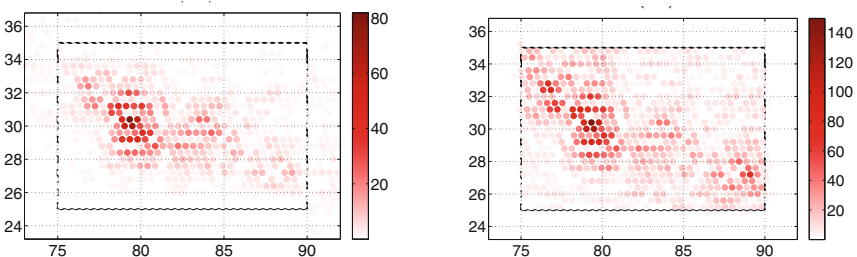


Fig. 9 Results from simulations with white noise added to the observations and the Abel-Poisson kernel: residuals in m^2/s^2 , values of the estimated coefficients \hat{d} , their standard deviation $\hat{\sigma}_d$, and their significance $|\hat{d}|/\hat{\sigma}_d$ derived with truncated singular value decomposition (column on the left) and prior information (column on the right)

to estimate parameters in a system with noisy observations, it shows its full benefits in the scenario with noise on the observations.

The Shannon low-pass kernel is a poor example, since in the noise-free case no reasonable values for the coefficients can be obtained. Also, the errors are fairly high. However, with prior information, the results are more promising. There is some correlation between the values of the coefficients and the signal, and the errors are comparably small. The error structures in the results from the non-band limited Abel-Poisson kernel (Fig. 9) are the same for both estimation methods and indicate that there are not enough grid points in the representation. The errors are high in the area of high signal energy, which cannot be completely modelled by the kernels. But nevertheless, the coefficients \mathbf{d} obtained via variance component estimation are highly correlated with the signal, and additionally, the coefficients in the margin have values close to zero and are not significant. This example of the non-truncated Abel-Poisson kernel thus shows the high importance of the spatial localization of the kernels in order to obtain physically meaningful coefficients. All the other kernels with side lobes and oscillations next to the main peak give coefficients \mathbf{d} which are less correlated with the signal, and still not zero or close to zero in the margin.

7 Summary and conclusions

In order to investigate different spherical radial basis functions and their performance in regional gravity field modelling, we set up a closed-loop simulation in which we estimate the coefficients for a representation of a given regional gravity signal in quasi-localizing radial basis functions and compare the synthesized signal from our representation to the original signal in terms of a cross-validation. We check different radial basis functions, which can all be represented in a Legendre expansion. Their performance in regional gravity modelling is evaluated by the relative error root mean square value and the correlation between the newly estimated coefficients and the signal to be represented. This correlation plays an important role because we are looking for physically meaningful solutions which can be used further to compute up- or downward continuation of the gravity signal or a different gravity functional. Our results show also, that a compromise between spatial and frequency localization of the radial basis function has to be found. This is seen from the errors and correlations of the estimated coefficients and the signal in the case of noise-contaminated observations when comparing the two extremes of our kernel selection, the Shannon band-pass kernel and the non-band limited Abel-Poisson kernel. The Shannon band-pass kernel filters exactly the bandwidth of the signal, and gives therefore the lowest errors, most of the noise can be filtered out. In contrast, the Abel-Poisson kernel provide the best spatial localization and, thus, the coefficients correlate the most with the signal. However, the errors are very high for the latter kernel. From the kernels which provide a compromise between these two we obtain very good results with the Blackman low pass kernel type I, the cubic polynomial kernel, and the truncated Abel-Poisson kernel. All these three kernels are low-pass filters and have a very smooth curve in the frequency domain for the transition from coefficients equal to one to coefficients which are zero. In the spatial domain they show oscillations, but the first side-lobes are much smaller than for the band-pass filtering kernels.

While in the global case, with spherical harmonics, the frequency localization is an important tool, since there is no spatial localization at all, both frequency and spatial localization have to be taken into account. A compromise between spatial and frequency localization has to be found. From the computations and examples we see that as long as the kernel is frequency limited, its actual frequency localization with respect to the signal bandwidth plays a minor role. The kernels' spatial behaviour is much more important for a good regional modelling result. To obtain physically meaningful coefficients a good spatial localization with small oscillations outside the main lobe of the kernel is required. The better the spatial localization of the kernel, the less is the leakage of signal outside the area of interest.

References

- Antoni, M., Keller, W., Weigelt, M.: Representation of regional gravity fields by radial base functions. In: *Observing our Changing Earth: Proceedings of the 2007 IAG General Assembly (International Association of Geodesy Symposia)*, vol. 133, pp. 293–299 (2009)
- Chambodut, A., Panet, I., Mandea, M., Diamant, M., Holschneider, M., Jamet, O.: Wavelet frames: an alternative to spherical harmonic representation of potential fields. *Geophys. J. Int.* **163**(3), 875–899 (2005). doi:[10.1111/j.1365-246X.2005.02754.x](https://doi.org/10.1111/j.1365-246X.2005.02754.x)
- ESA: Gravity field and steady-state ocean circulation mission. Reports for mission selection: the four candidate earth explorer core missions, ESA SP-1233(1) (1999)
- Fehlinger, T.: Multiscale formulations for the disturbing potential and the deflections of the vertical in locally reflected physical geodesy. Dissertation, University of Kaiserslautern, Department of Mathematics, Verlag Dr. Hut. ISBN 978-3-86853-213-5 (2009)
- Fehlinger, T., Freeden, W., Gramsch, S., Mayer, C., Michel, D., Schreiner, M.: Local modelling of sea surface topography from (geostrophic) ocean flow. *ZAMM* **87**(11–12), 775–791 (2007)
- Fischer, D.: Sparse regularization of a joint inversion of gravitational data and normal mode anomalies. University of Siegen, Dissertation (2011)
- Freeden, W., Michel, V.: *Multiscale Potential Theory With Applications to Geoscience*. Springer Basel AG (2004). ISBN 081764105X
- Freeden, W., Schreiner, M.: Spaceborne gravitational field determination by means of locally supported wavelets. *J. Geod.* **79**, 431–446 (2005). doi:[10.1007/s00190-005-0482-x](https://doi.org/10.1007/s00190-005-0482-x)
- Freeden, W., Schreiner, M.: Local multiscale modelling of geoid undulations from deflections of the vertical. *J. Geod.* **79**, 641–651 (2006)
- Freeden, W., Gervens, T., Schreiner, M.: *Constructive Approximation on the Sphere With Applications to Geoscience*. Oxford Science Publications (1998). ISBN 019853682
- Freeden, W., Fehlinger, T., Klug, M., Mathar, D., Wolf, K.: Classical globally reflected gravity field determination in modern locally oriented multiscale framework. *J. Geod.* **83**, 1171–1191 (2009). doi:[10.1007/s00190-009-0335-0](https://doi.org/10.1007/s00190-009-0335-0)
- Gerhards, C.: Spherical multiscale methods in terms of locally supported wavelets: theory and application to geomagnetic modeling. University of Kaiserslautern, Department of Mathematics, Dissertation (2012)
- Hofmann-Wellenhof, B., Moritz, H.: *Physical Geodesy*. Springer Wien, New York (2005)
- Holschneider, M., Chambodut, A., Mandea, M.: From global to regional analysis of the magnetic field on the sphere using wavelet frames. *Phys. Earth Planet. Inter.* **135**(2–3), 107–124 (2003). doi:[10.1016/S0031-9201\(02\)00210-8](https://doi.org/10.1016/S0031-9201(02)00210-8)
- Klees, R., Tenzer, R., Prutkin, I., Wittwer, T.: A data-driven approach to local gravity field modelling using spherical radial basis functions. *J. Geod.* **82**(8) (2008). doi:[10.1007/s00190-007-0196-3](https://doi.org/10.1007/s00190-007-0196-3)
- Koch, K.R.: Parameter estimation and hypothesis testing in linear models. Springer, Berlin (1999)
- Koch, K.R., Kusche, J.: Regularization of geopotential determination from satellite data by variance components. *J. Geod.* **76**, 259–268 (2002). doi:[10.1007/s00190-002-0245-x](https://doi.org/10.1007/s00190-002-0245-x)
- Moritz, H.: *Advanced Physical Geodesy*, 2nd edn. Wichmann Verlag, Karlsruhe (1989)
- Panet, I., Jamet, O., Diamant, M., Chambodut, A.: Modelling the earth's gravity field using wavelet frames. In: Jekeli, C., Bastos, L., Fernandes, J., Sansò, F. (eds.) *Gravity, Geoid and Space Missions*, International Association of Geodesy Symposia, vol. 129. Springer, Berlin, pp. 48–53 (2005)

- Panet, I., Kuroishi, Y., Holschneider, M.: Wavelet modelling of the gravity field by domain decomposition methods: an example over Japan. *Geophys. J. Int.* **184**(1), 203–219 (2010). doi:[10.1111/j.1365-246X.2010.04840.x](https://doi.org/10.1111/j.1365-246X.2010.04840.x)
- Press, W.H., Flanner, B.P., Teukolsky, S.A., Vetterling, W.T.: Numerical recipes: the art of scientific computing. Cambridge University Press, Cambridge (2007)
- Schmidt, M., Fengler, M., Mayer-Gürr, T., Eicker, A., Kusche, J., Sánchez, L., Han, S.C.: Regional gravity modeling in terms of spherical base functions. *J. Geod.* **81**(1), 17–38 (2007). doi:[10.1007/s00190-006-0101-5](https://doi.org/10.1007/s00190-006-0101-5)
- Tenzer, R., Klees, R.: The choice of the spherical radial basis functions in local gravity field modeling. *Stud. Geophys. Geod.* 1–18 (2007)
- Wolf, K.: Multiscale modeling of classical boundary value problems in physical geodesy by locally supported wavelets. Dissertation, University of Kaiserslautern, Department of Mathematics, Verlag Dr. Hut, ISBN 978-3-86853-249-4 (2009)